THE JOURNAL OF PHYSICAL CHEMISTRY B

Article

Cite This: J. Phys. Chem. B 2018, 122, 1484−1494

pubs.acs.org/JPCB

Graph−Theoretic Analysis of Monomethyl Phosphate Clustering in Ionic Solutions

Kyungreem Han,[†] Richard M. Venable,[†] Anne-Marie Bryant,[‡] Christopher J. Legacy,[‡] Rong Shen,[§] Hui Li,[§] Benoît Roux,[§] Arne Gericke,[‡] and Richard W. Pastor*[,†]

[†]Laboratory of Computational Biology, National Heart, Lung, and Blood Institute, National Institutes of Health, Bethesda, Maryland 20892, United States

[‡]Department of Chemistry and Biochemistry, Worcester Polytechnic Institute, Worcester, Massachusetts 01609, United States

[§]Department of Biochemistry and Molecular Biology, The University of Chicago, Chicago, Illinois 60637, United States

Supporting Information

ABSTRACT: All-atom molecular dynamics simulations combined with graph−theoretic analysis reveal that clustering of monomethyl phosphate dianion (MMP^{2-}) is strongly influenced by the types and combinations of cations in the aqueous solution. Although Ca^{2+} promotes the formation of stable and large MMP^{2-} clusters, K^+ alone does not. Nonetheless, clusters are larger and their link lifetimes are longer in mixtures of K^+ and Ca^{2+}. This "synergistic" effect depends sensitively on the Lennard-Jones interaction parameters between Ca^{2+} and the phosphorus oxygen and correlates with the hydration of the clusters. The pronounced MMP^{2-} clustering effect of Ca^{2+} in the presence of K^+ is confirmed by Fourier transform infrared spectroscopy. The characterization of the cation-dependent clustering of MMP^{2-} provides a starting point for understanding cation-dependent clustering of phosphoinositides in cell membranes.

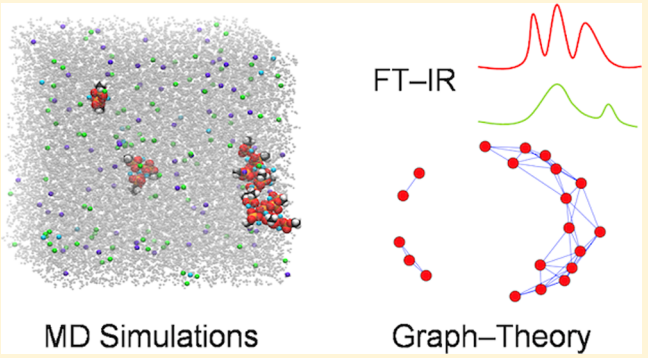

1. INTRODUCTION

Phosphatidylinositol (4,5)-bisphosphate ($PI(4,5)P_2$), a phosphorylated derivative of phosphatidylinositol, is a lipid in cell membranes that is critical for a broad range of cellular processes.[1,2] $PI(4,5)P_2$ binds to physiologically important proteins, including epsin N-terminal homology, AP180 N-terminal homology, four-point-one, ezrin, radixin, moesin, and pleckstrin homology domains.[3−5] The products of $PI(4,5)P_2$ hydrolysis by phosphoinositide-specific phospholipase C, inositol (1,4,5)-trisphosphate (IP_3) and diacylglycerol, function as key second messengers in numerous cellular signaling pathways.[2,6] Phosphorylation of $PI(4,5)P_2$ by PI 3-kinase (PI3K) leads to the formation of phosphatidylinositol-3,4,5-trisphosphate ($PI(3,4,5)P_3$), which is an integral part of the PI3K/Akt cell survival signaling pathway. $PI(4,5)P_2$ is also involved in the downregulation of the $PI(3,4,5)P_3$ signal because it binds and allosterically activates phosphatase and tensin homolog deleted on chromosome 10, which is the phosphatase that converts $PI(3,4,5)P_3$ back to $PI(4,5)P_2$.[7,8] Phosphoinositide−protein interactions are governed by the physicochemical properties of the phosphoinositide headgroup, which engages in ionic interactions as well as hydrogen bond formation with the protein targets. Corruptions in the interactions of phosphoinositides with their respective protein targets are associated with a range of disease states.[9] By virtue of its strong electrostatic nature, the interaction of phosphoinositides with various protein targets is strongly affected by pH and the ionization state of the bisphosphate group. It is therefore critically important for our understanding of phosphoinositide function to delineate the latter in environments that mimic biological membranes.

Many cellular processes mediated by phosphoinositides involve clustering of the lipid as well as colocalization with other lipids.[10,11] This is facilitated by the rich chemical functionality of the phosphoinositide headgroup. The phosphate groups can occupy different positions on the inositol ring (the general designation PIP_2 refers to isomers $PI(4,5)P_2$, $PI(3,4)P_2$, and $PI(3,5)P_2$), and their ionization states range between −1 and −2.[12] However, the structure of $PI(4,5)P_2$ clusters is not simply determined by the properties of single $PI(4,5)P_2$[1,2] or proteins that bind to the cluster.[3−5,13,14] Electrostatic interactions between $PI(4,5)P_2$ and ions are critical,[15−19] given that the net charge of $PI(4,5)P_2$ is −4 at pH 7.0.[20] Although it has been suggested that intra- and intermolecular hydrogen bond formation stabilizes $PI(4,5)P_2$ clusters by screening the charge at the phosphate

Received: October 30, 2017
Revised: December 30, 2017
Published: January 2, 2018

DOI: 10.1021/acs.jpcb.7b10730
J. Phys. Chem. B 2018, 122, 1484−1494

groups,[15,21−24] stable and large PI(4,5)P_2-clusters will only be able to form if the negative charges on PI(4,5)P_2 headgroups are adequately screened by soluble mono- and divalent cations, such as K^+ and Ca^{2+}. This assumption is supported by recent studies showing that the formation of PI(4,5)P_2 clusters highly depends on the local cation concentrations in pure PI(4,5)P_2 or PI(4,5)P_2-rich mixed membranes.[5,17−19,25] These findings are also consistent with observations from Langmuir film experiments that surface areas of PI(4,5)P_2 monolayers drop upon addition of mono- and divalent cations.[16,18] Although the electrostatic interactions between PI(4,5)P_2 molecules and cations have been extensively studied both experimentally and computationally since the late 1950s, the underlying mechanisms involved in cation-induced PI(4,5)P_2 cluster formation are not yet understood.[15,17,18,25−36]

The present study investigates clustering of monomethyl phosphate dianion (MMP^{2-}; Figure 1) in solutions of KCl,

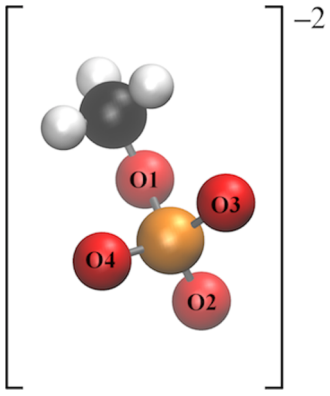

Figure 1. Structure of the monomethyl phosphate dianion (MMP^{2-}). Coloring: hydrogen, white; carbon, black; oxygen, red; phosphorus, orange.

$CaCl_2$, and a mixture of both cations as an entry point to modeling clustering of PI(4,5)P_2 in membranes. The results are generated using all-atom molecular dynamics (MD) simulations, analyzed using graph theory, and supported by Fourier transform infrared (FTIR) spectroscopy. It should be noted that the phosphomonoesters of the PI(4,5)P_2 headgroup show a biphasic pH-dependent ionization behavior. At pH 7.0, both completely deprotonated (MMP^{2-}) and single deprotonated phosphomonoester (monomethyl phosphate anion, MMP^-) exist.[12,15,22] However, cations mainly bind to the more negatively charged oxygen atoms of the phosphate dianions and therefore MMP^{2-} is the natural starting point for a study of PIP_2 clustering.

Graph−theoretic tools were used to characterize the clusters. Graph representations have a long history in chemistry,[37,38] and recently graph theory has been used to examine the physical properties of molecular clusters from both experiments and MD simulations.[39−41] Although in these previous studies graph−theoretic tools were successfully used to identify clusters, this study focuses on characterizing the structural and dynamical properties of the clusters.

The MD simulations were carried out using the general lipid and ion parameters in the Chemistry at Harvard Molecular Mechanics (CHARMM) C36 force field, as well as newly developed pairwise-specific Lennard-Jones (LJ) parameters for Ca^{2+} ions with Cl^- and phosphate oxygens. This modification involves substituting the default LJ parameters for the pair of atoms i and j constructed using the Lorentz−Berthelot combination rule,[42] $E_{min}^{(i,j)} = (E_{min}^{(i,i)}E_{min}^{(j,j)})^{1/2}$ and $R_{min}^{(i,j)} = (R_{min}^{(i,i)} + R_{min}^{(j,j)})/2$, by pairwise-specific LJ parameters (referred to by the keyword NBFIX in the CHARMM force field for nonbonded fix) to match additional experimental data, such as osmotic pressure.[43] In previous applications, the modified pairwise-specific NBFIX radius has typically been slightly larger than the default, which has the effect of reducing ion binding to a particular ligand or membrane surface.[44] It is shown here that an increase in radius counterintuitively leads to an increase in cluster size. Furthermore, a synergistic effect for cluster formation in Ca^{2+} and K^+ mixtures is observed.

By way of outline, Section 2 describes the simulation methods (Section 2.1), development of revised LJ parameters (Section 2.2), relevant graph theory (Section 2.3), and experimental procedures (Sections 2.4 and 2.5). Section 3 begins with an examination of convergence. This is essential to establish given the slow rearrangement of the ions around MMP^{2-}. The parameters necessary for the graph theory (such as coordinates for each vertex and the distance threshold for defining edges between vertices) are obtained from simulation in Section 3.2, and the clustering analysis is carried out in Section 3.3. The results of FTIR spectroscopy of solutions of MMP^{2-}, KCl, and $CaCl_2$ are presented in Section 3.4. Section 4 combines the Discussion and Conclusions.

2. METHODS

2.1. Simulations. Table 1 lists the five systems simulated in this study. All contain 20 MMP^{2-} (a concentration of

Table 1. MD Systems

		systems (cubic, $L \approx 68$ Å)				
	MMP^{2-}	Ca^{2+}	K^+	Cl^-	water	force field
S1	20		140	100	10 407	C36
S2	20	70		100	10 481	C36
S3	20	70		100	10 481	C36/NBFIX
S4						
a	20	35	70	100	10 439	C36
b	20	35	70	100	10 438	C36
c	20	35	70	100	10 439	C36
S5						
a	20	35	70	100	10 439	C36/NBFIX
b	20	35	70	100	10 438	C36/NBFIX
c	20	35	70	100	10 439	C36/NBFIX

approximately 100 mM) and KCl (∼500 mM, S1), $CaCl_2$ (∼250 mM, S2 and S3), or both cations (∼250 mM KCl and ∼125 mM $CaCl_2$, S4 and S5). The systems with two cations manifested higher variability compared to those with only one type and were therefore simulated in triplicate.

MMP^{2-} and ions were randomly placed and minimized in vacuum. Then, the systems were solvated using preequilibrated TIP3 water boxes. Water molecules with oxygens within 2.0 Å of the previously placed MMP^{2-} or ions were deleted. Accordingly, different systems have slightly different numbers of water molecules. Systems were minimized using the steepest descent algorithm, heated to 293.15 K over 40 ps, and then simulated to 600 ns under constant number, pressure, and temperature (NPT) at 293.15 K and 1 atm using the Hoover thermostat. The integration time step was 1 fs, and coordinate sets were saved every 5 ps. Electrostatics were evaluated using particle mesh Ewald (PME) with ca. one grid point per

DOI: 10.1021/acs.jpcb.7b10730
J. Phys. Chem. B 2018, 122, 1484−1494

angstrom (Å), a sixth-order spine interpolation for the complementary error function, a κ value of 0.32, and a 12 Å real space cutoff. The van der Waals term used a standard 6−12 LJ form, with force-switched truncation over the range 8−12 Å. The SHAKE constraint method was applied to all covalent bonds to hydrogen, with the default 1.0×10^{-10} Å tolerance. The CHARMM (c41b1) program[45] was used for the MD simulations. The CHARMM C36 force field[46−48] was used for MMP^{2-} and ions, and TIP3P for water;[49] this is designated by the abbreviation "C36" here. Simulations S3 and S5 were carried out with pair-specific LJ parameters adjusted to reproduce the experimental osmotic pressure accurately for a wide range of concentrations, as described in the next subsection. Results from this set of simulations include the label NBFIX when necessary for clarity, e.g., C36/NBFIX.

2.2. Revision of Lennard-Jones Parameters. Pair-specific LJ parameters of Ca^{2+} with Cl^- and with the carbonyl oxygen of the phosphate group (NBFIX) were optimized to fit experimentally measured osmotic pressures for salt solutions of calcium chloride ($CaCl_2$) and calcium dimethyl phosphate ($Ca[DMP]_2$) according to the method developed by Luo and Roux.[43] DMP^- is a model compound commonly used to represent the phospholipid polar headgroup.[47,48] The osmolality of the solutions was measured using the Vapro vapor pressure osmometer (Wescor, Inc.; model 5520). The instrument was calibrated using 100, 290, and 1000 mmol/kg sodium chloride standard solutions and had passed the clean test before the measurements. The $CaCl_2$ solutions were prepared from 2.0 M calcium chloride dehydrate solution (Hampton Research, ≥99.5%), and the $Ca[DMP]_2$ solutions were prepared by the neutralization of calcium hydroxide (Fisher Scientific, 98%) and dimethyl phosphate (Fisher Scientific, 98%) at room temperature. All of the reagents were used without further purification. Ten measurements were performed for each solution, and the mean value was used in the osmotic pressure MD simulations.

Osmotic pressures were calculated from all-atom MD simulations using the method developed by Luo and Roux.[43] The starting configurations of the simulation systems were constructed by randomly inserting a specific number of solute molecules into an orthorhombic water box ($45 \times 45 \times 90$ Å^3) with its center fixed at the origin. Although the solvent water molecules are allowed to move freely throughout the entire simulation system, the solute molecules are restrained by two virtual semipermeable membranes located at $Z = \pm 22.5$ Å, implemented via a flat-bottom half-harmonic planar potential with a force constant of 10 kcal/mol/Å^2. Hence, the central $45 \times 45 \times 45$ Å^3 region of the simulated system serves as an aqueous solution, whereas the rest of the system contains only pure water.[43] Each osmotic pressure simulation system was first equilibrated for 5 ns in the NPT ensemble. The simulation temperature was maintained at 300 K using a Langevin thermostat, and the pressure was set at 1 atm using the Nosé−Hoover Langevin piston method with a constant cross-sectional area in the x−y plane. The last frame was then used as the starting point for five independent production simulations with different initial velocities. Production simulations of 50 ns each were carried out in the NVT ensemble with a constant temperature of 300 K maintained by Langevin dynamics. These MD simulations were performed using the NAMD simulation package[50] with an integration time step of 2 fs. Electrostatic interaction was evaluated using the particle mesh Ewald (PME) method with a grid density of at least 1/Å^3, and the van der Waals interactions were smoothly switched off (10−12 Å). Periodic boundary conditions were imposed in all directions. Trajectories of the production simulations were saved every 1000 steps for data analysis.

Figure 2 plots the experimental and calculated osmotic pressures for $CaCl_2$ and $Ca[DMP]_2$. The default and optimized

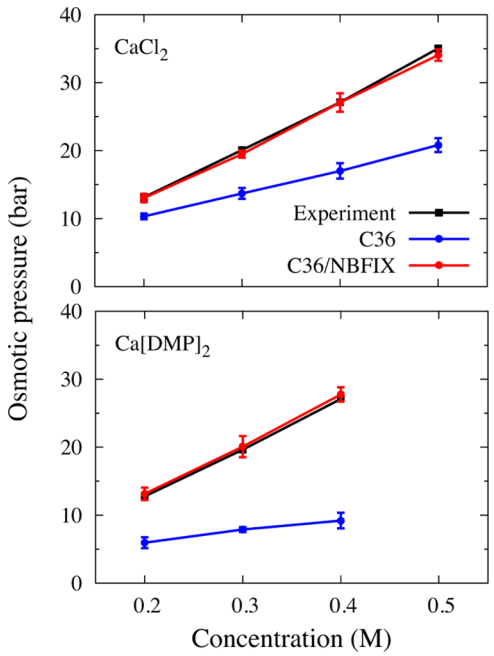

Figure 2. Comparison of osmotic pressure from experiment and simulations with the default C36 parameters and C36/NBFIX for aqueous solutions of calcium chloride (top) and calcium dimethyl phosphate (DMP^-) (bottom).

Table 2. Lennard-Jones Parameters[a]

atom	pair	default		NBFIX	
		$E_{min}(i,j)$ (kcal/mol)	$R_{min}(i,j)$ (Å)	$E_{min}(i,j)$ (kcal/mol)	$R_{min}(i,j)$ (Å)
CAL	CLA	−0.134164	3.637	−0.134164	3.727
CAL	OG2P1	−0.120	3.067	−0.120	3.256

[a]The default LJ parameters E_{min} and $R_{min}/2$ are −0.120 kcal/mol and 1.367 Å for CAL; −0.150 kcal/mol and 2.27 Å for CLA; and −0.12 kcal/mol and 1.70 Å for OG2P1.

LJ parameters are listed in Table 2. For the sake of simplicity, the default value for the LJ well depth E_{min} was kept unchanged by the optimization. The osmotic pressure simulated from the default LJ parameters constructed using the Lorentz−Berthelot combination rule and obtained from the pair-specific (NBFIX) optimized LJ parameters are shown in Figure 2 under the headings C36 and C36/NBFIX, respectively. Although the default LJ parameters yield severely underestimated osmotic pressures in concentrated aqueous solutions for both $CaCl_2$ and $Ca[DMP]_2$, the optimized LJ (C36/NBFIX) fit the experimental data very well. The underestimated osmotic pressure is generally indicative of an excess of ion pairing, reflecting cation−anion interactions that are slightly too favorable.[43] Compared to the default LJ parameters, the optimized pair-specific R_{min} of CAL−CLA is increased by 0.090 Å, and the R_{min}

DOI: 10.1021/acs.jpcb.7b10730
J. Phys. Chem. B 2018, 122, 1484−1494

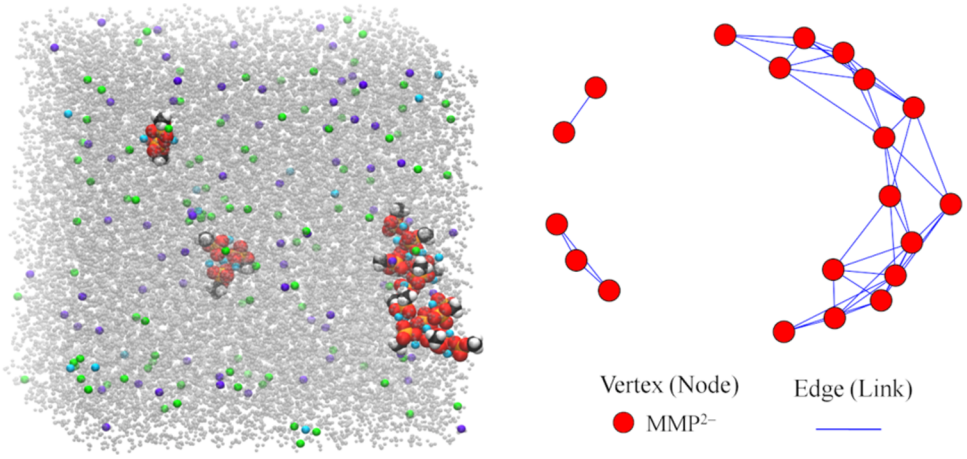

Figure 3. Snapshot (400 ns, left) and its graphical representation (right) from simulation S5a (K^+ and Ca^{2+} generated with the C36 force field with adjusted calcium LJ parameters (NBFIX)). MMP^{2-} molecules are approximately doubled in size for better visibility in the left panel, and coloring is the same as in Figure 1: water is gray, Ca^{2+} is cyan, K^+ is violet, and Cl^- is green. The graph consists of MMP^{2-} as vertices (red) and edges between them (solid lines).

of CAL−OG2P1 is increased by 0.189 Å. The small increase in the R_{min} is sufficient to reduce the ion−ligand interaction, leading to a smaller number of ion pairs in concentrated solution.

2.3. Graph−Theoretic Analysis. Molecular graphs for MMP^{2-} clusters were constructed with each phosphorus atom defining the distance between adjacent MMP^{2-}. Vertices (nodes) were taken to be connected to each other by an edge (link) if the distance between the phosphorus atoms was less than the distance threshold of 8 Å, based on the phosphorus−phosphorus radial distribution functions ($g(r)$ P−P) evaluated from the MD simulations (see Section 3.2). The major interactions between neighboring phosphorus atoms occur within this threshold.

The mathematical representation of a graph is the $N \times N$ adjacency (connectivity) matrix $\boldsymbol{A}$, in which N is the number of vertices in the graph. The elements of the matrix, $\boldsymbol{A}_{ij}$, are as follows

$\boldsymbol{A}_{ij} = 1$ if i and j are linked,

$\boldsymbol{A}_{ij} = 0$ otherwise,

$\boldsymbol{A}_{ij} = 0$ for $i = j$ (no self-loops)

The weight (strength of the interaction) and directionality of the edges were not considered in this study. The adjacency matrix was converted to the geodesic distance matrix via the Floyd−Warshall algorithm[51,52] for selected analyses.

The adjacency matrix was used to obtain the vertex degree k (the number of edges incident to the vertex), average degree $\langle k \rangle$ ($k = 0$ is included in the average), degree distribution $P(k)$, edge lifetime distribution, and clustering coefficient C.[53,54] $\langle k \rangle$ is a general descriptor of the overall connectivity and stationarity of a system. $P(k)$ is one of the more robust tools for capturing the underlying organizing principles of a graph, i.e., how vertices and edges are organized, and the edge lifetime distribution provides useful insights into the dynamical properties of a graph.[53−58] However, additional measures are required to characterize clusters, given that more than one cluster size distribution can be consistent with the same $\langle k \rangle$ or even the same $P(k)$. For example, a system with many small clusters could have the same $\langle k \rangle$ as one with several large clusters and many isolated vertices ($k = 0$). Graphs of similar $P(k)$ can have different cluster sizes/structures.[53,59] The clustering coefficient C provides the necessary discrimination. C is the average of all local clustering coefficients c_i in the graph.[55−58] The local clustering coefficient of each vertex c_i is defined as the ratio of the number of connections among the k_i neighbors of a given vertex i to its maximum possible value, $k_i(k_i - 1)/2$.

Other clustering indices (i.e., cluster size, graph size, % MMP^{2-} within the clusters) were derived from the geodesic distance matrix. Within graph theory, a cluster can be defined as a group of connected vertices such that every vertex is linked by one or more edges to one or more vertices in the cluster. The cluster size denotes the number of vertices in a particular cluster. The graph size denotes the number of vertices in all of the clusters. The % MMP^{2-} within the clusters denotes percent ratio of the graph size and the total numbers of vertices.

The creation of the adjacency and geodesic distance matrices from MD trajectories was aided by the open source C and R package ChemNetworks.[38] Analyses were carried with the help of the Python package NetworkX,[60] tailored scripts, or ChemNetworks.

2.4. Synthesis of Bis(cyclohexylamine) Monomethyl Phosphate. According to the literature,[61] dicholoromethyl phosphate **1** (1 mol equiv) in acetonitrile (0.5 mL per mmol of **1**) was added dropwise to a solution of $AgNO_3$ (2 mol equiv) in water/acetonitrile (1:1, v/v, 1.5 mL per g of $AgNO_3$) with stirring at 0 °C. The mixture was stirred overnight in a refrigerator and filtered several times to remove the AgCl precipitate. The solvent was evaporated under reduced pressure. Ethanol was added to the residue to complete precipitation of AgCl. After filtration, the ethanol was removed under reduced pressure and the resulting residue was placed under high vacuum. Monomethyl phosphate **2** was obtained as a colorless oil with white crystals (confirmed with ^{31}P NMR and ^1H NMR). Cyclohexylamine was added to **2** in excess at 0 °C to form insoluble bis(cyclohexylamine) monomethyl phosphate **3**. Excess cyclohexamine was removed via filtration, and **3** was sonicated in hexane, resulting in a white solid. The white solid **3** was dried overnight under vacuum. The monomethyl phosphate salt **3** was characterized by ^{31}P NMR H decoupling (chemical shift: 4.84 ppm in D_2O) and ^1H NMR

DOI: 10.1021/acs.jpcb.7b10730
J. Phys. Chem. B 2018, 122, 1484−1494

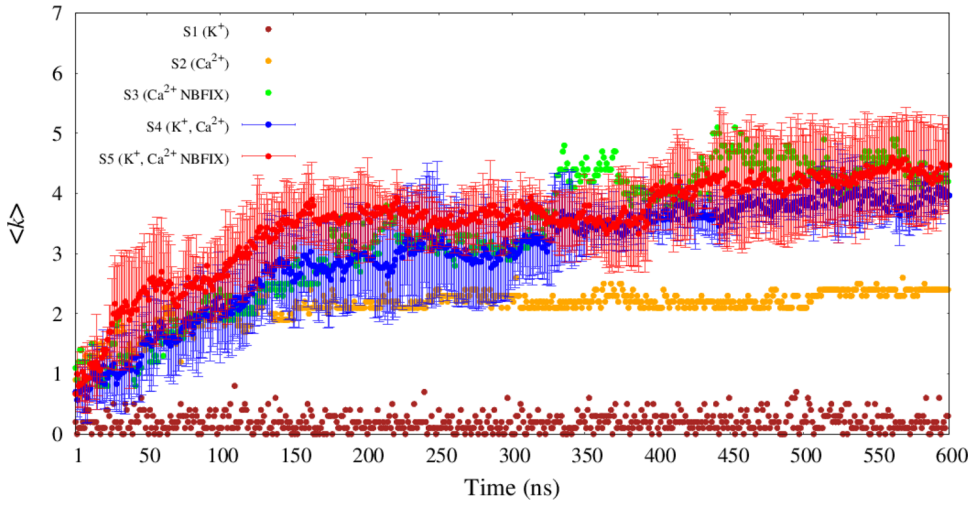

Figure 4. Time evolution of average vertex degree $\langle k \rangle$ for MMP^{2-} graphs. The results of three replicates for each parameter set for the mixed system (S4 and S5) are presented as means (filled circles) and standard deviations (error bars).

(chemical shifts: 1.18 (m), 1.32 (m), 1.65 (m), 1.79 (m), 1.87 (m), 3.08 (m), and 3.46 (d) ppm in D_2O) and FTIR bands in the spectral region 900−1600 cm^{-1}.

2.5. Monomethyl Phosphate Interaction with Ca^{2+} and K^+ Ions Using in Situ FTIR. In situ FTIR measurements were performed on a Mettler Toledo ReactIR 15 instrument using a 6.3 mm AgXDi Comp probe and iC IR software. A pH-dependent titration was performed with 400 mg of monomethyl phosphate dissolved in 4 mL of high-performance liquid-chromatography-grade water by adding HCl dropwise to obtain spectra over the desired pH range. On the basis of this titration, a titration of Ca^{2+} ions into monomethyl phosphate dissolved in an excess K^+ was performed at pH 7.5, the deprotonated state of monomethyl phosphate. To have an excess of K^+ ions, 400 mg of bis(cyclohexylamine) salt was dissolved in 4 mL of 2.5 M KCl solution (~1:7 (MMP^{2-}: K^+) molar ratio, which is consistent with simulations). The pH was adjusted to 7.5 using HCl and stirred at room temperature. Then, 200 μL additions of 0.5 M $CaCl_2$ were titrated into the solution at 3 min intervals. For each Ca^{2+} concentration, a spectrum of 250 scans was obtained with a 4 cm^{-1} resolution. Peak positions were determined from the 2nd derivative of the respective spectrum using a center of mass algorithm.

3. RESULTS

3.1. Overall Connectivity and Convergence. In the following descriptions, systems will be denoted by the relevant cation or the abbreviation in Table 1, and are understood to contain Cl^- and MMP^{2-} (see Table 1 for a complete description).

Figure 3 shows the 400 ns snapshot (left) and graph (right) from S5a, one of the replicates containing K^+ and Ca^{2+}. There are three clusters consisting of 2, 3, and 15 MMP^{2-}. The average vertex degree $\langle k \rangle$ is obtained here by counting the number of links for each vertex (MMP^{2-}) and dividing by 20. Each MMP^{2-} in the dimer has one link, those in the trimer have two links, and those in the largest cluster have three to seven links, yielding $\langle k \rangle$ = 4.3.

Figure 4 plots the time evolution of $\langle k \rangle$ of graphs for each system. The system with only K^+ (S1) converged within a nanosecond. Those with Ca^{2+} required from 150 ns (S2) to 400 ns (S3−S5). The 400−600 ns segments of all trajectories are used for most of the analyses presented here.

It is evident from Figure 4 that K^+ and Ca^{2+} have dramatically different effects on MMP^{2-} connectivity: K^+ with C36 (S1) displays little connectivity ($\langle k \rangle = 0.21 \pm 0.01$); Ca^{2+} with C36 (S2) is intermediate ($\langle k \rangle = 2.3 \pm 0.1$); and Ca^{2+} with C36/NBFIX (S3) has the most ($\langle k \rangle = 4.4 \pm 0.1$). There is a striking increase in connectivity to $\langle k \rangle = 3.8 \pm 0.2$ when Ca^{2+} and K^+ for C36 are combined (S4) compared to the pure Ca^{2+} (S2). But this trend is not observed with C36/NBFIX (S5), where $\langle k \rangle = 4.2 \pm 0.4$. Overall, S3 and S5 yield similar $\langle k \rangle$, but as will be shown below, their cluster size distributions are different.

The radial distribution functions between MMP^{2-} ($g(r)$ P−P in Figure 5), those between cation and phosphate oxygen ($g(r)$ Ca^{2+}−O and $g(r)$ K^+−O in Figures S1 and S2), and between cation and water ($g(r)$ Ca^{2+}−W and $g(r)$ K^+−W in Figures S3 and S4) are also well converged by 400 ns.

3.2. Interactions between MMP^{2-} Molecules. The interactions between cations and the oxygen atoms of MMP^{2-} vary depending on the types of cations, their combinations, and force field parameters. In all cases, Ca^{2+} shows greater binding affinities to oxygen atoms than K^+. Figures S1 and S2 show that as the simulations with both cations (S4 and S5) equilibrated, Ca^{2+} accumulated in the first coordination shells and expelled K^+. These figures also show that the distances corresponding to the maximum peaks of $g(r)$ for Ca^{2+} were shorter than those of K^+, and the distances for Ca^{2+} from simulations with C36 were shorter than those from C36/NBFIX for Ca^{2+}.

Coordination numbers were evaluated by setting r = 3 Å in

$$I(r) = \int_0^r 4\pi r'^2 \rho g(r')\, dr' \quad (1)$$

where ρ is the bulk density; $I(r)$ at other values of r provides a useful measure of trends in coordination and structure. As shown in the right panels of Figure S1, the coordination number is 0.4 for K^+ (S1), 1.3 for Ca^{2+} with C36 (S2), and 1.5 for Ca^{2+} with C36/NBFIX (S3). The different coordination numbers and maximum peak distances between cations and phosphorus oxygens lead to structural and dynamical differences in the MMP^{2-} clusters on a larger scale, as partially

DOI: 10.1021/acs.jpcb.7b10730
J. Phys. Chem. B 2018, 122, 1484−1494

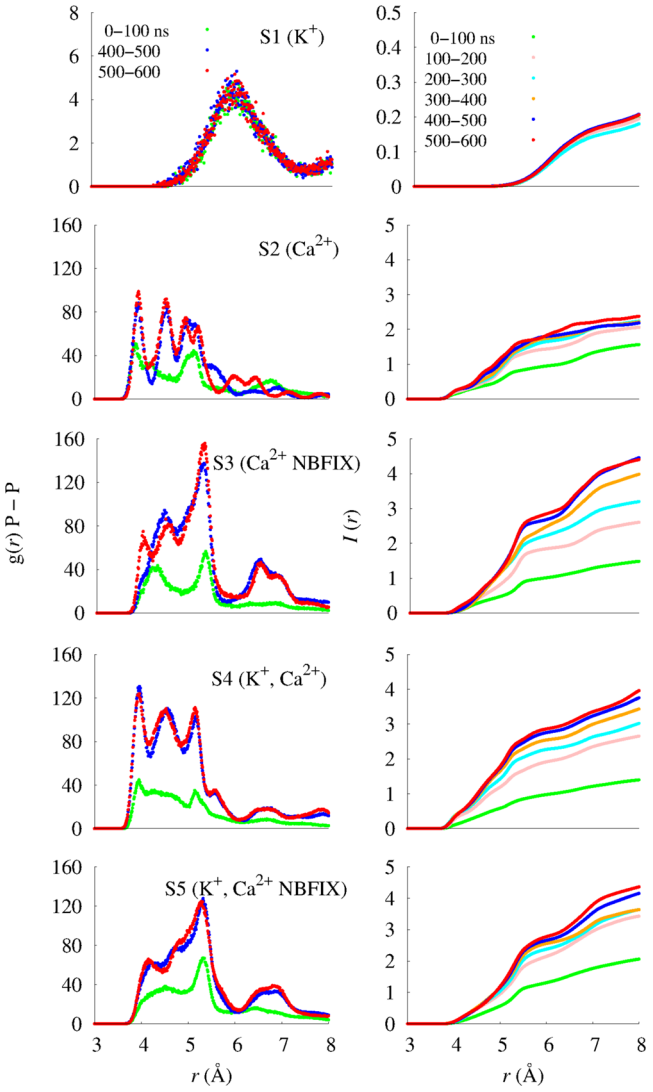

Figure 5. Radial distribution functions $g(r)$ P−P between adjacent phosphorus atoms of MMP^{2-} molecules (left), and the integrated radial distribution function $I(r)$ (right).

revealed by the $g(r)$ P−P profiles between adjacent MMP^{2-} molecules (Figure 5).

The P−P radial distribution functions of the systems with only Ca^{2+} (S2 and S3; the second and third rows in Figure 5) or both K^+ and Ca^{2+} (S4 and S5; the fourth and fifth rows) exhibited multiple overlapping small peaks. In contrast, the system with only K^+ (S1; the first row) showed a single dominant peak with relatively low amplitude. $I(r)$ values for the systems including Ca^{2+} were much larger than those of the system with only K^+, indicating larger clusters. Distances corresponding to major peaks of the systems, including Ca^{2+}, were shorter than those of the system with only K^+, indicating tighter binding.

The $g(r)$ P−P from simulations with C36 (S2 and S4) displayed three distinct peaks, whereas those from C36/NBFIX (S3 and S5) showed double peaks. $I(r)$ values of the system with only Ca^{2+} from C36 (S2) were substantially lower than those of the system with only Ca^{2+} from C36/NBFIX (S3). However, when K^+ was combined with Ca^{2+} (S4), the $I(r)$ from C36 increased to similar values as the systems with C36/NBFIX (S3 and S5). This is consistent with the trends in system connectivity ($\langle k \rangle$) (Figure 4).

3.3. Clustering Analysis. Figure 6 displays the cluster size distributions of MMP^{2-} graphs. Cluster sizes of systems with

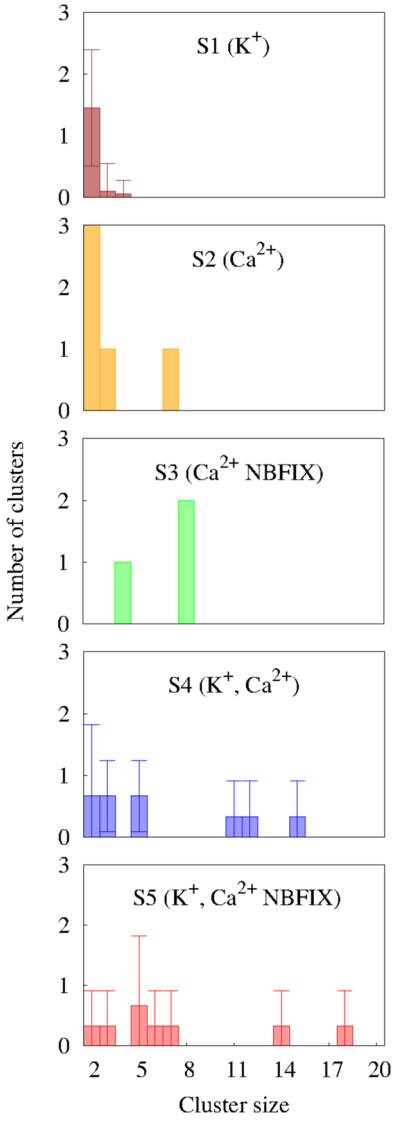

Figure 6. Cluster size distributions. The result of the system with only K^+ was obtained by taking averages over the last 20 ns trajectories (580−600 ns) because the clusters in this system were very short-lived (see Figure 8); otherwise, the 600 ns time point is represented. The error bars for S1 denote standard deviation over time (20 ns simulations). The results of two cation systems for each parameter set (S4 and S5) are presented as means and standard deviations.

only Ca^{2+} (S2 and S3) were much larger than those from the system consisting of only K^+ (S1). S1 exhibited mostly MMP^{2-} dimers (the largest cluster size was only 4 during the last 20 ns of the simulations). As shown in Table 3, the graph size of the system at 600 ns was only 6, indicating that 14 (isolated) vertices did not participate in the cluster formation. Accordingly, the % MMP^{2-} within the clusters was only 30. In contrast, those clustering indices for systems of only Ca^{2+} were much greater than the only K^+ system. For example, the clustering coefficient C of S1 equaled 0, whereas C = 0.58 and 0.79 for S2 and S3, respectively.

DOI: 10.1021/acs.jpcb.7b10730
J. Phys. Chem. B 2018, 122, 1484−1494

Table 3. Clustering Indexes[a]

system	graph size	% MMP^{2-} within the clusters	average cluster size	clustering coefficient C
S1	6	30	2.00	0.00
S2	16	80	3.20	0.58
S3	20	100	6.67	0.79
S4	19.3 ± 0.6	96.7 ± 2.9	6.4 ± 0.2	0.78 ± 0.16
S5	20.0 ± 0.0	100.0 ± 0.0	8.3 ± 2.9	0.73 ± 0.18

[a]These clustering indices were calculated for the 600 ns snapshot. Calculations on the two cation systems (S4 and S5) were carried out in triplicate, and the results are presented as means and standard deviations.

As implied from the $g(r)$ P−P profiles (Figure 5), cluster size (Figure 6) and clustering indices (Table 3) are greater for S3 than S2. However, the clustering tendency is comparable for the mixed cation systems (S4 and S5), as measured by graph size, % MMP^{2-} within the clusters, average cluster size, and clustering coefficient. Furthermore, giant clusters (i.e., cluster size > 15) are observed only from the systems with two cations. The effect of K^+ on MMP^{2-} clustering in the two cation systems is more pronounced for C36.

Figures 7 and 8 show the time-averaged degree distributions $P(k)$ and edge lifetime distributions, respectively.[53−58] $P(k)$ for S1 is exponential with very low probabilities for vertices with multiple edges (1.70 and 0.25% for k = 2 and 3, respectively), that is, there were no strongly connected hubs in this system. The edges had short lifetimes (∼1 ns), which are exponentially distributed.

In contrast, the system with only Ca^{2+} under C36 (S2) showed two distinct patterns of $P(k)$: the relatively slowly decaying power-law degree distribution for low-degree vertices as compared to S1 and the right-skewed distributions for high-degree vertices. The edge lifetime distribution exhibited power-law decay with fat tails. The existence of such edges with long lifetimes in the fat tails, together with high-degree vertices could play essential roles in the formation of large and stable clusters. Although the total occurrence of edges during the (last) 450 ns simulations for S2 (208) was much lower than that of S1 (779), the resulting clusters in S2 were much larger and more stable, indicating that edges with long lifetimes are more important for the formation of large and stable clusters.

S3 shows a right-skewed Weibull distribution (third row in Figure 7). This characteristic degree distribution of this system is qualitatively different from S2, implying that the underlying organization of vertices and edges of those systems are fundamentally different.

The systems with two cations also exhibited the Weibull degree distributions with a considerable amount of high-degree vertices in fat tails (i.e., k > 8) (fourth and fifth rows in Figure 7). In addition, the edge lifetime distributions exhibited power-law decays with edges having long lifetimes in relatively greater numbers than those in the systems with only Ca^{2+} (Figure 8).

3.4. Infrared Spectroscopy of Monomethyl Phosphate. Figure 9 compares the FTIR spectra of monomethyl phosphate in the presence of K^+ (2.5 M) pH 7.5 with the corresponding spectra in the presence of increasing concentrations of Ca^{2+}. The spectrum of monomethyl phosphate at pH 7.5 in the presence of 2.5 M K^+ is typical for the completely deprotonated MMP^{2-}. At 1082 and 1111 cm^{-1}, a band doublet that has been assigned to $\nu_a(PO_3^{2-})$ and ν(C−O−(P)) stretching vibrations is observed.[62] At 981 cm^{-1}, $\nu_s(PO_3^{2-})$ is

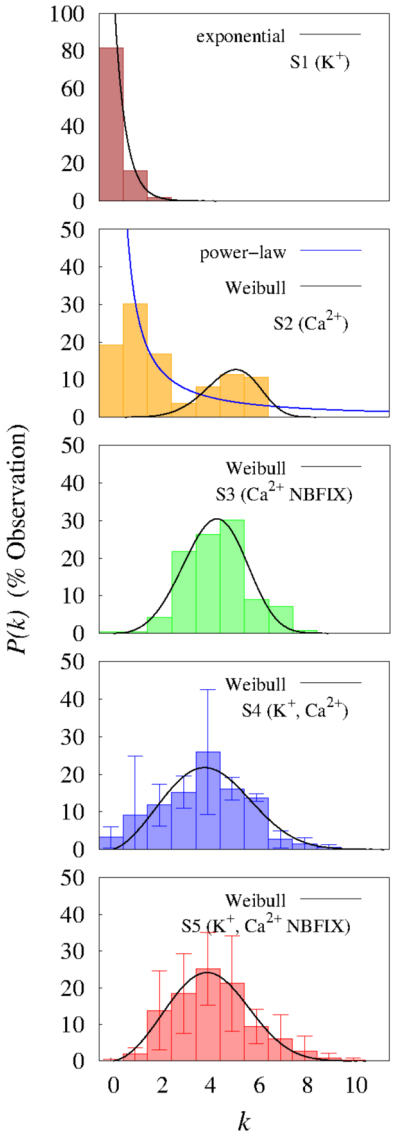

Figure 7. Degree distributions and best statistical fits (for k > 0). The degree distribution $P(k)$ denotes the frequency of occurrence of vertices with degree k between 400 and 600 ns. Results of two cation systems (S4 and S5) are presented as the mean and standard deviation (error bars).

found (for the pH-dependent spectra of monomethyl phosphate between pH 1.5 and pH 10 (Figure S5)). Upon addition of Ca^{2+} ions, a white precipitate is observed, indicating the formation of Ca^{2+}/MMP^{2-} crystals. This crystallization is characterized by a marked shift of the MMP^{2-} band positions. In the higher wave number region, two strong bands develop at 1093 and 1138 cm^{-1}, respectively. The $\nu_s(PO_3^{2-})$ band found in the absence of Ca^{2+} at 981 cm^{-1} loses intensity with increasing Ca^{2+} concentration and instead, a band at 1033 cm^{-1} with a shoulder at 1007 cm^{-1} develops. It has been proposed that the binding of Ca^{2+} to MMP^{2-} reduces the symmetry group from C_{3v} (symmetric and asymmetric PO_3^{2-} stretching vibrations doubly degenerate) to a low symmetry group, where the degeneracy is removed. Therefore, the 1138 and 1093 cm^{-1} bands have been assigned to the asymmetric stretching vibrations of the PO_3^{2-} group, whereas the bands at 1033 and 1007 cm^{-1} are due to the PO_3^{2-} symmetric stretching mode in the MMP^{2-}/Ca^{2+} complex.[62] Overall, this demon-

DOI: 10.1021/acs.jpcb.7b10730
J. Phys. Chem. B 2018, 122, 1484−1494

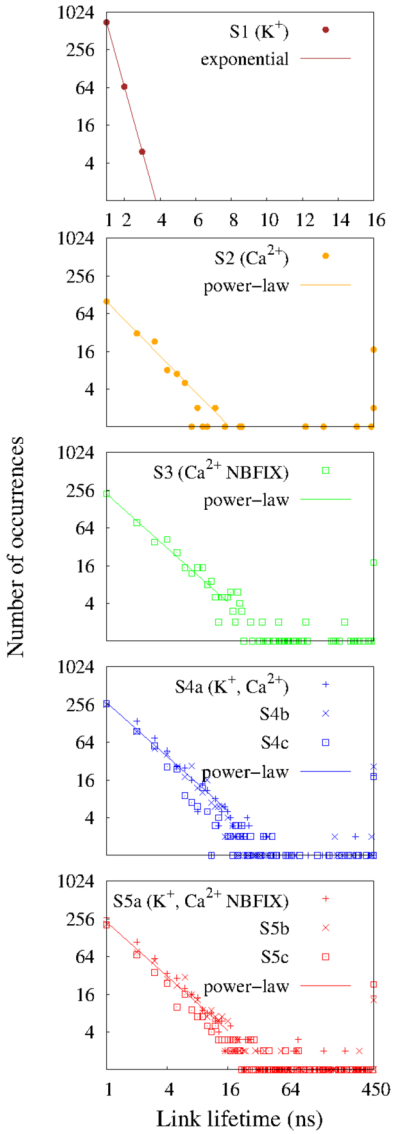

Figure 8. Edge lifetime distributions and best statistical fits; these results were obtained from the last 450 ns of each simulations to include the very long lifetimes.

strates that the interaction of Ca^{2+} with MMP^{2-} is significantly stronger than the interaction of K^+ with MMP^{2-} and that Ca^{2+} bridges two or more MMP^{2-} molecules for a broad Ca^{2+} concentration range. The experiment with low and high Ca^{2+} concentrations will more likely correspond to the simulations with two cations and only Ca^{2+}, respectively, in terms of local cation concentration around MMP^{2-}. With the high Ca^{2+} concentrations (e.g., 0.198 M [Ca^{2+}]), the first coordination shell of MMP^{2-} can be mostly occupied by Ca^{2+}.

4. DISCUSSION AND CONCLUSIONS

This study investigated the clustering behavior of MMP^{2-} in K^+ and Ca^{2+} solutions with all-atom MD simulations and graph–theoretic analysis. The characterization of the MMP^{2-} interaction with K^+ and/or Ca^{2+} informs the analysis of cation-dependent clustering of lipids with phosphomonoester groups like phosphoinositides or phosphatidic acid. Using MMP^{2-} significantly reduces the complexity and cost of computations and thereby enhances the speed and accuracy of the computations of the formation of spontaneous cation-

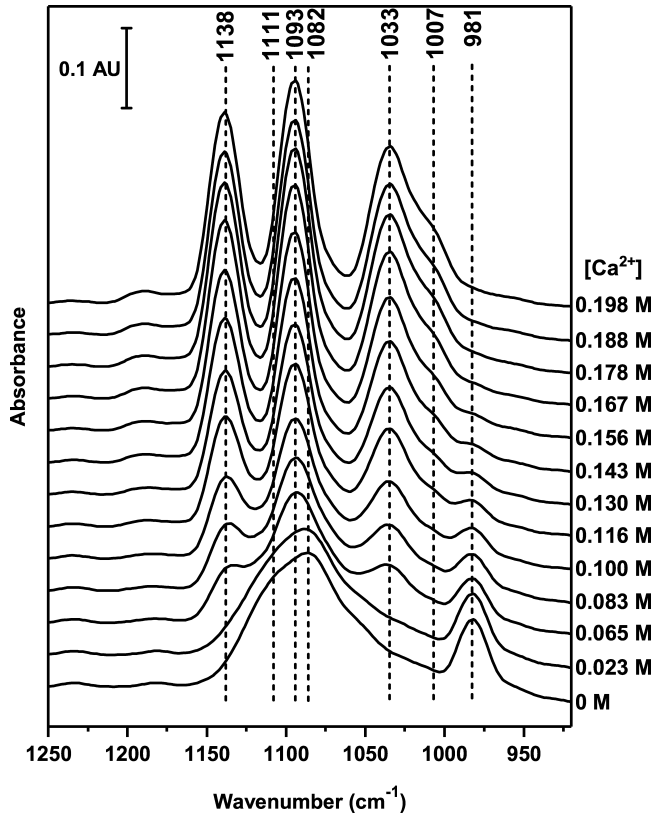

Figure 9. Infrared spectra of MMP^{2-}. FTIR spectra of monomethyl phosphate were measured in the presence of K^+ (2.5 M) with increasing concentrations of Ca^{2+}. The spectrum of monomethyl phosphate at pH 7.5 in the presence of 2.5 M K^+ is typical for the completely deprotonated monomethyl phosphate, i.e., MMP^{2-}.

bridged MMP^{2-} aggregates (i.e., dimers/trimers). Electrostatic interactions developed among adjacent $PI(4,5)P_2$, ions,[15−19,27,29] peripheral proteins,[1,3−5,7,8,13,14] and related signaling molecules[2,6,63] can then extend the aggregates to large and stable clusters. Characterizing the interactions of MMP^{2-} with cations and the resulting structural and dynamical properties of MMP^{2-} clusters should provide a better understanding of the multiplicity and context dependency of $PI(4,5)P_2$ clusters in biological membranes.

The simulations were carried out using newly developed Lennard-Jones interaction parameters for calcium and chloride and for calcium and phosphate oxygens. The new parameter set, termed C36/NBFIX, yielded excellent agreement with experimental osmotic pressure over a wide range of concentrations for solutions of calcium chloride and calcium dimethyl phosphate (Figure 2).

The analysis began with the radial distribution function $g(r)$ P−P and its integral $I(r)$ (Figure 5). The first peak of $g(r)$ provides a good measure of the optimal binding (or interaction) distance and relative binding strength; peaks at larger distances show the patterns of clustering, akin to a fingerprint. $I(r)$ to each minimum yields the coordination numbers of successive shells. The $g(r)$ for MMP^{2-}−MMP^{2-} in the solution with only K^+ has only a single small peak at 6 Å, whereas solutions with Ca^{2+} (solely or with K^+) show three or more large peaks between 4 and 8 Å in $g(r)$. Systems simulated with the C36 force field parameters for Ca^{2+} (S2 and S4) have shorter P−P distances than those simulated with C36/NBFIX (S3 and S4), a modification that slightly increases the LJ

DOI: 10.1021/acs.jpcb.7b10730
J. Phys. Chem. B 2018, 122, 1484−1494

minimum distance between calcium and the oxygen atoms of MMP^{2-} (the interaction terms between MMP^{2-} are unchanged). $I(r)$ values at 8 Å are comparable for systems with K^+ and Ca^{2+} (S4 and S5) and with Ca^{2+} only with C36/NBFIX (S3); these are approximately twice as large as for the systems with only Ca^{2+} with C36 (S2).

The clustering of MMP^{2-} in Ca^{2+} (S2 and S3) is opposite to that observed for DMP^-, where simulations with C36 yielded lower osmotic pressure (consistent with increased aggregation) than simulations with C36/NBFIX (Figure 2). This result highlights an important difference between these two methyl phosphates. Although DMP^- is a good model for phospholipids with phosphodiester linked headgroups, it does not provide substantial insight into phosphoinositide clustering.

The preceding results do not provide information on the structure and dynamics of the clusters. Hence, the detailed structural and dynamic properties of the MMP^{2-} clusters were examined with graph−theoretic approaches. Figure 6 clearly shows the differences in cluster sizes implied by the $g(r)$ P−P profiles. Ca^{2+} induced clustering, whereas clustering in the system with only K^+ is minimal (mostly dimers). However, there is a significant synergistic effect of K^+ on cluster formation: the largest clusters (>15) appear only in the systems with both cations (S4 and S5) and are twice the size as those with only Ca^{2+} (S3 and S4). This effect is masked when only considering the average number of edges, where $\langle k \rangle$ is the same for S3, S4, and S5 (Figure 4).

Figures 7 ($P(k)$) and 8 (edge lifetimes) examine the characteristics of the clusters for each system. $P(k)$ of a random (molecular) graph exhibits a Poisson distribution with a peak at $P(\langle k \rangle)$ indicating no organizing principles. If $P(k)$ is exponential, power-law, log−normal, or Weibull (so called characteristic curves), one can infer that there exist underlying principles of the architecture of the graph (Figure 7). The edge lifetime distribution is an indicator of the dynamical properties of clusters, such as clustering stability and dynamical reorganization (Figure 8). The observation that the system with only K^+ (S1) exhibited only unstable small clusters could be related to the dominance of low-degree vertices and short-edge lifetimes. Systems with only Ca^{2+} (S2 and S3) showed a relatively slow decay of the degree- and edge lifetime distributions, which could promote the formation of large and stable clusters. The organizations of vertices and edges of S2 and S3 are fundamentally different as revealed by different $P(k)$. Likewise, the development of cluster sizes >15 and the stronger clustering tendencies of the systems with K^+/Ca^{2+} mixtures are consistent with their characteristic right-skewed degree distributions with considerable amounts of high-degree vertices and slowly decaying edge lifetimes. The infrared spectroscopy data also confirmed the strong MMP^{2-} clustering effect of Ca^{2+} in the presence of K^+ (Figure 9).

The mechanism of how ions induce/stabilize phosphate clusters is not yet clear. Why are some ions more effective than others, and how do different ions work synergistically? This question also arises in the study of DNA and RNA folding, where stabilization by ions can be both direct and water-mediated.[64−67] A pertinent observation from the present study is that K^+ mostly resides at the surface of the clusters, with only a small fraction located in the first coordination shell of the MMP^{2-}. The synergistic effect of K^+ may then be related to mechanisms other than the direct interaction between K^+ and MMP^{2-}, such as hydration. As shown in Figures S3 and S4, Ca^{2+} is significantly less hydrated in simulations with C36 (3.86 for S2 and 2.82 for S4) than for C36/NBFIX (5.62 for S3 and 4.28 for S5). K^+ is well hydrated, with seven waters in its first hydration shell (Figure S4). This raises the possibility that the weakly interacting monovalent cation recruits water to the cluster and modulates the strong electrostatic interactions between the Ca^{2+} and phosphate oxygen atoms to yield larger clusters. The mutual interaction of phosphoinositides is a delicate balance between charge−charge repulsive and attractive forces due to direct or water-mediated hydroxyl/hydroxyl and/or phosphate/hydroxyl hydrogen bond formation. The presence of water in these clusters, promoted by K^+, may lead to a stronger clustering because the bridging effect of Ca^{2+} is augmented by the formation of hydrogen bonds. The synergistic effect is not observed with the C36 default Ca^{2+} model because it binds more strongly to the phosphate oxygen atoms and is consequently less hydrated.

■ ASSOCIATED CONTENT

Supporting Information

The Supporting Information is available free of charge on the ACS Publications website at DOI: 10.1021/acs.jpcb.7b10730.

Radial distribution functions of cations, and spectra of monomethyl phosphate (PDF)

■ AUTHOR INFORMATION

Corresponding Author

*E-mail: pastorr@nhlbi.nih.gov. Phone: +1 (301) 435-2035. Fax: +1 (301) 480-6496.

ORCID

Kyungreem Han: 0000-0002-2290-4858
Benoît Roux: 0000-0002-5254-2712
Arne Gericke: 0000-0002-3682-0241
Richard W. Pastor: 0000-0002-2454-5131

Notes

The authors declare no competing financial interest.

■ ACKNOWLEDGMENTS

The authors thank Alexander MacKerell, Jr., for ongoing discussions regarding the force field. This research was supported by the Intramural Research Program of the National Institutes of Health, National Heart, Lung, and Blood Institute, and utilized the high-performance computational capabilities at the National Institutes of Health, Bethesda, MD (NHLBI LoBoS cluster). Dr. Han's research was supported by a grant from the KRIBB Research Initiative Program (Korean Biomedical Scientist Fellowship Program), Korea Research Institute of Bioscience and Biotechnology, Republic of Korea. Dr. Gericke's research was supported by the NSF Chemistry Division (CHE 1508499). The work of Drs. Li, Rong, and Roux was supported by the NIH through grant R01 GM072558.

■ REFERENCES

(1) McLaughlin, S.; Murray, D. Plasma Membrane Phosphoinositide Organization by Protein Electrostatics. *Nature* **2005**, *438*, 605−611.

(2) Balla, T. Phosphoinositides: Tiny Lipids with Giant Impact on Cell Regulation. *Physiol. Rev.* **2013**, *93*, 1019−137.

(3) Lemmon, M. A. Phosphoinositide Recognition Domains. *Traffic* **2003**, *4*, 201−213.

(4) Lemmon, M. A. Pleckstrin Homology (PH) Domains and Phosphoinositides. *Biochem. Soc. Symp.* **2007**, *74*, 81−93.

DOI: 10.1021/acs.jpcb.7b10730
J. Phys. Chem. B 2018, 122, 1484−1494

(5) Lemmon, M. A. Membrane Recognition by Phospholipid-Binding Domains. *Nat. Rev. Mol. Cell Biol.* **2008**, *9*, 99−111.
(6) Czech, M. P. PIP2 and PIP3: Complex Roles at the Cell Surface. *Cell* **2000**, *100*, 603−606.
(7) Pulido, R.; Baker, S. J.; Barata, J. T.; Carracedo, A.; Cid, V. J.; Chin-Sang, I. D.; Dave, V.; den Hertog, J.; Devreotes, P.; Eickholt, B. J.; et al. A Unified Nomenclature and Amino Acid Numbering for Human PTEN. *Sci. Signaling* **2014**, *7*, No. pe15.
(8) Lee, J.-O.; Yang, H.; Georgescu, M.-M.; Di Cristofano, A.; Maehama, T.; Shi, Y.; Dixon, J. E.; Pandolfi, P.; Pavletich, N. P. Crystal Structure of the PTEN Tumor Suppressor: Implications for Its Phosphoinositide Phosphatase Activity and Membrane Association. *Cell* **1999**, *99*, 323−334.
(9) Liu, Y.; Bankaitis, V. A. Phosphoinositide Phosphatases in Cell Biology and Disease. *Prog. Lipid Res.* **2010**, *49*, 201−217.
(10) Brown, D. A. PIP2Clustering: From Model Membranes to Cells. *Chem. Phys. Lipids* **2015**, *192*, 33−40.
(11) Golebiewska, U.; Kay, J. G.; Masters, T.; Grinstein, S.; Im, W.; Pastor, R. W.; Scarlata, S.; McLaughlin, S. Evidence for a Fence that Impedes the Diffusion of Phosphatidylinositol 4,5-Bisphosphate Out of the Forming Phagosomes of Macrophages. *Mol. Biol. Cell* **2011**, *22*, 3498−3507.
(12) Graber, Z. T.; Thomas, J.; Johnson, E.; Gericke, A.; Kooijman, E. E. Effect of H-Bond Donor Lipids on Phosphatidylinositol-3,4,5-Trisphosphate Ionization and Clustering. *Biophys. J.* **2018**, *114*, 126−136.
(13) van den Bogaart, G.; Meyenberg, K.; Risselada, H. J.; Amin, H.; Willig, K. I.; Hubrich, B. E.; Dier, M.; Hell, S. W.; Grubmüller, H.; Diederichsen, U.; Jahn, R. Membrane Protein Sequestering by Ionic Protein-Lipid Interactions. *Nature* **2011**, *479*, 552−555.
(14) Harishchandra, R. K.; Neumann, B. M.; Gericke, A.; Ross, A. H. Biophysical Methods for the Characterization of PTEN/Lipid Bilayer Interactions. *Methods* **2015**, *77*−*78*, 125−135.
(15) Graber, Z. T.; Gericke, A.; Kooijman, E. E. Phosphatidylinositol-4,5-Bisphosphate Ionization in the Presence of Cholesterol, Calcium or Magnesium Ions. *Chem. Phys. Lipids* **2014**, *182*, 62−72.
(16) Graber, Z. T.; Wang, W.; Singh, G.; Kuzmenko, I.; Vaknin, D.; Kooijman, E. E. Competitive Cation Binding to Phosphatidylinositol-4,5-Bisphosphate Domains Revealed by X-Ray Fluorescence. *RSC Adv.* **2015**, *5*, 106536−106542.
(17) Wang, Y.-H.; Slochower, D. R.; Janmey, P. A. Counterion-Mediated Cluster Formation by Polyphosphoinositides. *Chem. Phys. Lipids* **2014**, *182*, 38−51.
(18) Slochower, D. R.; Wang, Y.-H.; Tourdot, R. W.; Radhakrishnan, R.; Janmey, P. A. Counterion-Mediated Pattern Formation in Membranes Containing Anionic Lipids. *Adv. Colloid Interface Sci.* **2014**, *208*, 177−188.
(19) Ellenbroek, W. G.; Wang, Y.-H.; Christian, D. A.; Discher, D. E.; Janmey, P. A.; Liu, A. J. Divalent Cation-Dependent Formation of Electrostatic PIP(2) Clusters in Lipid Monolayers. *Biophys. J.* **2011**, *101*, 2178−2184.
(20) McLaughlin, S.; Wang, J.; Gambhir, A.; Murray, D. PIP2 and Proteins: Interactions, Organization, and Information Flow. *Annu. Rev. Biophys. Biomol. Struct.* **2002**, *31*, 151−175.
(21) Kooijman, E. E.; Gericke, A. Physical Chemistry and Biophysics of Polyphosphoinositide Mediated Lipid Signaling. *Chem. Phys. Lipids* **2014**, *182*, 1−2.
(22) Kooijman, E. E.; King, K. E.; Gangoda, M.; Gericke, A. Ionization Properties of Phosphatidylinositol Polyphosphates in Mixed Model Membranes. *Biochemistry* **2009**, *48*, 9360−9371.
(23) Jiang, Z.; Redfern, R. E.; Isler, Y.; Ross, A. H.; Gericke, A. Cholesterol Stabilizes Fluid Phosphoinositide Domains. *Chem. Phys. Lipids* **2014**, *182*, 52−61.
(24) Graber, Z. T.; Jiang, Z.; Gericke, A.; Kooijman, E. E. Phosphatidylinositol-4,5-Bisphosphate Ionization and Domain Formation in the Presence of Lipids with Hydrogen Bond Donor Capabilities. *Chem. Phys. Lipids* **2012**, *165*, 696−704.
(25) Bilkova, E.; Pleskot, R.; Rissanen, S.; Sun, S.; Czogalla, A.; Cwiklik, L.; Róg, T.; Vattulainen, I.; Cremer, P. S.; Jungwirth, P.; Coskun, Ü. Calcium Directly Regulates Phosphatidylinositol 4,5-Bisphosphate Headgroup Conformation and Recognition. *J. Am. Chem. Soc.* **2017**, *139*, 4019−4024.
(26) Catte, A.; Girych, M.; Javanainen, M.; Loison, C.; Melcr, J.; Miettinen, M. S.; Monticelli, L.; Maatta, J.; Oganesyan, V. S.; Ollila, O. H. S.; Tynkkynen, J.; Vilov, S. Molecular Electrometer and Binding of Cations to Phospholipid Bilayers. *Phys. Chem. Chem. Phys* **2016**, *18*, 32560−32569.
(27) Wang, Y.-H.; Collins, A.; Guo, L.; Smith-Dupont, K. B.; Gai, F.; Svitkina, T.; Janmey, P. A. Divalent Cation-Induced Cluster Formation by Polyphosphoinositides in Model Membranes. *J. Am. Chem. Soc.* **2012**, *134*, 3387−3395.
(28) Slochower, D. R.; Wang, Y. H.; Radhakrishnan, R.; Janmey, P. A. Physical Chemistry and Membrane Properties of Two Phosphatidylinositol Bisphosphate Isomers. *Phys. Chem. Chem. Phys.* **2015**, *17*, 12608−12615.
(29) Slochower, D. R.; Huwe, P. J.; Radhakrishnan, R.; Janmey, P. A. Quantum and All-Atom Molecular Dynamics Simulations of Protonation and Divalent Ion Binding to Phosphatidylinositol 4,5-Bisphosphate (PIP(2). *J. Phys. Chem. B* **2013**, *117*, 8322−8329.
(30) Edsall, J. T.; Wyman, J. *Biophysical Chemistry*; Academic Press: NY, 1958; Vol. *1*.
(31) Hendrickson, H. S.; Fullington, J. G. Stabilities of Metal Complexes of Phospholipids: Ca(II), Mg(II), and Ni(II) Complexes of Phosphatidylserine and Triphosphoinositide*. *Biochemistry* **1965**, *4*, 1599−1605.
(32) Dawson, R. M. C. 'Phosphatido-Peptide'-like Complexes Formed by the Interaction of Calcium Triphosphoinositide with Protein. *Biochem. J.* **1965**, *97*, 134−138.
(33) Folch, J.; Lees, M.; Stanley, G. H. S. A Simple Method for the Isolation and Purification of Total Lipids from Animal Tissues. *J. Biol. Chem.* **1957**, *226*, 497−509.
(34) Hauser, H.; Dawson, R. M. C. The Binding of Calcium at Lipid-Water Interfaces. *Eur. J. Biochem.* **1967**, *1*, 61−69.
(35) Toner, M.; Vaio, G.; McLaughlin, A.; McLaughlin, S. Adsorption of Cations to Phosphatidylinositol 4,5-Bisphosphate. *Biochemistry* **1988**, *27*, 7435−7443.
(36) Park, Y.; Seo, J. B.; Fraind, A.; Pérez-Lara, A.; Yavuz, H.; Han, K.; Jung, S.-R.; Kattan, I.; Walla, P. J.; Choi, M.; et al. Synaptotagmin-1 Binds to PIP(2)-Containing Membrane but not to SNAREs at Physiological Ionic Strength. *Nat. Struct. Mol. Biol.* **2015**, *22*, 815−823.
(37) Trinajstic, N. *Chemical Graph Theory*, 2nd ed.; CRC Press: FL, 1992.
(38) Ozkanlar, A.; Clark, A. E. ChemNetworks: A Complex Network Analysis Tool for Chemical Systems. *J. Comput. Chem.* **2014**, *35*, 495−505.
(39) Tenney, C. M.; Cygan, R. T. Analysis of Molecular Clusters in Simulations of Lithium-Ion Battery Electrolytes. *J. Phys. Chem. C* **2013**, *117*, 24673−24684.
(40) Choi, J.-H.; Cho, M. Ion Aggregation in High Salt Solutions. II. Spectral Graph Analysis of Water Hydrogen-Bonding Network and Ion Aggregate Structures. *J. Chem. Phys.* **2014**, *141*, No. 154502.
(41) Choi, J.-H.; Cho, M. Ion Aggregation in High Salt Solutions. IV. Graph-Theoretical Analyses of Ion Aggregate Structure and Water Hydrogen Bonding Network. *J. Chem. Phys.* **2015**, *143*, No. 104110.
(42) Allen, M. P.; Tildesley, D. J. *Computer Simulation of Liquids*; Clarendon Press: NY, 1987.
(43) Luo, Y.; Roux, B. Simulation of Osmotic Pressure in Concentrated Aqueous Salt Solutions. *J. Phys. Chem. Lett.* **2010**, *1*, 183−189.
(44) Venable, R. M.; Luo, Y.; Gawrisch, K.; Roux, B.; Pastor, R. W. Simulations of Anionic Lipid Membranes: Development of Interaction-Specific Ion Parameters and Validation Using NMR Data. *J. Phys. Chem. B* **2013**, *117*, 10183−10192.
(45) Brooks, B. R.; Bruccoleri, R. E.; Olafson, B. D.; States, D. J.; Swaminathan, S.; Karplus, M. CHARMM: A Program for Macromolecular Energy, Minimization, and Dynamics Calculations. *J. Comput. Chem.* **1983**, *4*, 187−217.

DOI: 10.1021/acs.jpcb.7b10730
J. Phys. Chem. B 2018, 122, 1484−1494

(46) Vanommeslaeghe, K.; Hatcher, E.; Acharya, C.; Kundu, S.; Zhong, S.; Shim, J.; Darian, E.; Guvench, O.; Lopes, P.; Vorobyov, I.; et al. CHARMM General Force Field (CGenFF): A Force Field for Drug-Like Molecules Compatible with the CHARMM All-Atom Additive Biological Force Fields. *J. Comput. Chem.* **2010**, *31*, 671−690.
(47) Pastor, R. W.; MacKerell, A. D. Development of the CHARMM Force Field for Lipids. *J. Phys. Chem. Lett.* **2011**, *2*, 1526−1532.
(48) Klauda, J. B.; Venable, R. M.; Freites, J. A.; O'Connor, J. W.; Tobias, D. J.; Mondragon-Ramirez, C.; Vorobyov, I.; MacKerell, A. D.; Pastor, R. W. Update of the CHARMM All-Atom Additive Force Field for Lipids: Validation on Six Lipid Types. *J. Phys. Chem. B* **2010**, *114*, 7830−7843.
(49) Jorgensen, W. L.; Chandrasekhar, J.; Madura, J. D.; Impey, R. W.; Klein, M. L. Comparison of Simple Potential Functions for Simulating Liquid Water. *J. Chem. Phys.* **1983**, *79*, 926−935.
(50) Phillips, J. C.; Braun, R.; Wang, W.; Gumbart, J.; Tajkhorshid, E.; Villa, E.; Chipot, C.; Skeel, R. D.; Kalé, L.; Schulten, K. Scalable Molecular Dynamics with NAMD. *J. Comput. Chem.* **2005**, *26*, 1781−1802.
(51) Floyd, R. W. Algorithm 97: Shortest path. *Commun. ACM* **1962**, *5*, 345.
(52) Warshall, S. A Theorem on Boolean Matrices. *J. Assoc. Comput. Mach.* **1962**, *9*, 11−12.
(53) Albert, R.; Barabási, A.-L. Statistical Mechanics of Complex Networks. *Rev. Mod. Phys.* **2002**, *74*, 47−97.
(54) Vázquez, A.; Pastor-Satorras, R.; Vespignani, A. Large-Scale Topological and Dynamical Properties of the Internet. *Phys. Rev. E* **2002**, *65*, No. 066130.
(55) Watts, D. J.; Strogatz, S. H. Collective Dynamics of 'Small-World' Networks. *Nature* **1998**, *393*, 440−442.
(56) Latora, V.; Marchiori, M. Efficient Behavior of Small-World Networks. *Phys. Rev. Lett.* **2001**, *87*, No. 198701.
(57) Barabási, A.-L.; Albert, R. Emergence of Scaling in Random Networks. *Science* **1999**, *286*, 509−512.
(58) Amaral, L. A. N.; Scala, A.; Barthélémy, M.; Stanley, H. E. Classes of Small-World Networks. *Proc. Natl. Acad. Sci. U.S.A.* **2000**, *97*, 11149−11152.
(59) Li, L.; Alderson, D.; Doyle, J. C.; Willinger, W. Towards a Theory of Scale-Free Graphs: Definition, Properties, and Implications. *Internet Math.* **2005**, *2*, 431−523.
(60) Hagberg, A. A.; Schult, D. A.; Swart, P. J. In *Exploring Network Structure, Dynamics, and Function Using NetworkX*, Proceedings of the 7th Python in Science Conference (SciPy 2008), 2008; pp 11−16.
(61) Modro, A. M.; Modro, T. A. An Improved Synthesis of Monoesters of Phosphoric-Acid. *Org. Prep. Proced. Int.* **1992**, *24*, 57−60.
(62) Laroche, G.; Dufourc, E. J.; Dufourcq, J.; Pezolet, M. Structure and Dynamics of Dimyristoylphosphatidic Acid/Calcium Complexes by Deuterium NMR, Infrared, and Raman Spectroscopies and Small-Angle X-Ray Diffraction. *Biochemistry* **1991**, *30*, 3105−3114.
(63) Liu, P.; Cheng, H.; Roberts, T. M.; Zhao, J. J. Targeting the Phosphoinositide 3-Kinase (PI3K) Pathway in Cancer. *Nat. Rev. Drug Discovery* **2009**, *8*, 627−644.
(64) Lavelle, L.; Fresco, J. R. Stabilization of Nucleic Acid Triplexes by High Concentrations of Sodium and Ammonium Salts Follows the Hofmeister Series. *Biophys. Chem.* **2003**, *105*, 681−699.
(65) Coman, D.; Russu, I. M. Site-Resolved Stabilization of a DNA Triple Helix by Magnesium Ions. *Nucleic Acids Res.* **2004**, *32*, 878−883.
(66) Hamelberg, D.; Williams, L. D.; Wilson, W. D. Effect of a Neutralized Phosphate Backbone on the Minor Groove of B-DNA: Molecular Dynamics Simulation Studies. *Nucleic Acids Res.* **2002**, *30*, 3615−3623.
(67) Draper, D. E.; Grilley, D.; Soto, A. M. Ions and RNA Folding. *Annu. Rev. Biophys. Biomol. Struct.* **2005**, *34*, 221−243.

DOI: 10.1021/acs.jpcb.7b10730
J. Phys. Chem. B 2018, 122, 1484−1494